

An Empirical Model Relating Pressure Drop and Mass Flow Rate in General Internal Flows: Theoretical Basis and Sensitivity Analysis

T. Pant and H. Wang[†]

School of Aeronautics and Astronautics, Purdue University West Lafayette, Indiana, 47907, USA.

[†]Corresponding Author Email: haifeng@purdue.edu

(Received August 22, 2017; accepted November 11, 2017)

ABSTRACT

An empirical model is evaluated that is in a very simple form and is often used in automobile industry to relate the pressure drop and mass flow rate in internal flows. Despite the simplicity of the model, it is remarkably accurate when it is used in a wide range of internal flows. Such accuracy and the theoretical basis of the model is not well understood, and this work aims to provide such an understanding. The theoretical basis of the empirical model is sought by performing an integral analysis based on the Navier-Stokes equation in a laminar developing channel flow. The analysis successfully yields a model that is in the same form as the empirical model. The accuracy and sensitivity of the model is then thoroughly examined through the computational studies of several internal flows. Two regimes of the model behavior in internal flows are identified, a convection dominated flow regime and a diffusion dominated flow regime. In each regime, the sensitivity of the model accuracy to the model parameters is found to be substantially different. Finally, the empirical model is applied to several more complicated internal flows to demonstrate the applicability of the model in general flows.

Keywords: Empirical model; Internal flows; Pressure drop, Mass flow rate, CFD, Sensitivity Analysis.

NOMENCLATURE

| | | | |
|------------|--|---------------|--------------------------------------|
| a, b | empirical model constants | u_b | bulk velocity |
| a^*, b^* | variables of derived model | u_{in} | uniform inlet velocity |
| A | cross-sectional area | u_τ | friction velocity |
| C_f | friction factor | u^+ | mean velocity in terms of wall units |
| d_1, d_2 | geometry constants of curved channel | u^{*+} | RMS velocity in x direction |
| H | height of straight channel | v | velocity in y direction |
| $H(x)$ | height of channel at x location | v^{*+} | RMS velocity in y direction |
| H_{in} | height of curved channel at inlet | W | width of straight channel |
| H_m | average height of converging channel | w^{*+} | RMS velocity in z direction |
| L | length of channel | | |
| \dot{m} | mass flow rate | Δp | pressure drop |
| \hat{n} | normal vector | ΔP | pressure drop across car underhood |
| $=$ | | ε | sensitivity input |
| p | mean pressure across a cross-section | ρ | density |
| Re | Reynolds number | μ | molecular viscosity |
| Re_τ | Reynolds number based on friction velocity | ν | kinematic viscosity |
| u | velocity in x direction | σ | deviation in pressure |
| u_0 | centerline velocity | σ^+ | positive deviation in pressure |
| | | σ^- | negative deviation in pressure |
| | | τ_w | wall shear stress |

1. INTRODUCTION

An empirical model that relates the pressure drop to

mass flow rate in internal flows has been widely used in the automobile industry (Personal communication, Bruno, D., Schwarze, M., and Zuck, B.,

BMW AG, Munich). Typically, the empirical model is written as (Pant *et al.* (2013), Pant (2014)):

$$\Delta p = am^2 + bm, \quad (1)$$

where Δp is the pressure drop inside a channel over some distance, \dot{m} is the mass flow rate through the channel and a, b are dimensional constants. Pressure drop along the flow direction in internal flows measures the loss of mechanical energy of fluid due to viscous dissipation and can be related to the entropy generation in fluid. An interesting entropy analysis of internal flows based on the second-law of thermodynamics can be found in Herwig and Schmandt (2013). The empirical model in Eq. (1) relates the pressure drop, which measures losses, to the mass flow rate. This can be used, for example, to estimate the mass flow rate through an auto-mobile underhood for cooling analysis (Pant *et al.*(2013), Pant (2014)). It is clarified that fully developed flow condition is not assumed in Eq. (1), and indeed it is found in this work that this model is surprisingly accurate for some highly developing internal flows.

Although the empirical model has been useful in engineering applications, to our best knowledge, it has not been studied in previous publications and the theoretical basis of the model remains unknown. This motivates this work, and the goal of this paper is to perform an analysis of the empirical model in Eq. (1) based on the theory of fluid mechanics (White (2008)) and to examine the accuracy and uncertainty of the model through numerical simulations in order to provide a theoretical basis to the model.

The empirical model in Eq. (1) is in a similar form to the Darcy-Forchheimer equation which is used for flows through porous media (Ward (1964), Ahmed and Sunada (1969), Lage *et al.* (2005), Straughan (2010), Liao *et al.* (2016)). Despite the similarity, the two models arise from two different contexts and the theoretical basis for the models is different. In this work, we focus on examining the fundamental basis of the empirical model in Eq. (1) in simple internal flows without porous medium. Both theoretical analysis and computational fluid dynamics (CFD) simulations will be performed to examine the empirical model in the contexts of both laminar and turbulent flows. The work is expected to be valuable in providing a sound theoretical basis to the empirical model that is useful not only in the automobile industry but also in engineering applications that involve internal flows such as pipe flows in the oil and gas industry (Dukler *et al.*(1964), Baker *et al.* (1953), Rodriguez and Oliemans (2006), Ghosh *et al.* (2009), Ouyang and Aziz (1996)) and heat exchangers in power generation and aerospace industries (Manglik and Bergles (1995), Wang *et al.* (1997), Muley and Manglik (1999), Junqi *et al.* (2007)). Additionally, the empirical model in Eq. (1) is expected to be useful for the development of measurement techniques for mass flow rate (Oliveira *et al.* (2009), Martin *et al.*(2006), Shodiya *et al.* (2012), Kim *et al.* (2005), Payne and O’Neal (2004)), and

for the design of ventilation systems in buildings (Hensen and Lamberts (2012), Awbi (2008)).

The rest of the paper is organized as follows. Section 2 performs an integral analysis of the empirical model based on the Navier-Stokes equation to establish a theoretical basis for the model. Section 3 examines the dependence of a model coefficient in the empirical model on the mass flow rate. This dependence directly determines the accuracy of the empirical model. Sensitivity analysis of the empirical model and the characterization of channel flows is then conducted in Section 3 to provide a thorough understanding of the empirical model over a wide range of conditions. The model’s performance is examined further in several internal flows in Section 4 to show the applicability of the empirical model to more general flows. The conclusions are drawn in Section 5.

2. NAVIER-STOKES EQUATION ANALYSIS OF THE EMPIRICAL MODEL

2.1 Analysis of Laminar Developing Channel Flow

To seek the theoretical basis of the empirical model in Eq. (1), we first consider a simple steady state, laminar, spatially developing channel flow as shown in Fig. 1. From this point onwards we perform an integral analysis of the channel flow based on the Navier-Stokes equation (White (2008)). The channel has length L and height H . The flow is assumed to be incompressible and all thermo-transport properties are assumed to be constant. The flow is two-dimensional and a unit width is considered in the span-wise direction so that the cross-sectional area of the channel is $A = H \times W$ where $W = 1\text{m}$. The governing equation for the momentum in the x direction can be written as (White (2008)),

$$\frac{\partial(uu)}{\partial x} + \frac{\partial(uv)}{\partial y} = -\frac{1}{\rho} \frac{\partial p}{\partial x} + \nu \frac{\partial^2 u}{\partial x^2} + \nu \frac{\partial^2 u}{\partial y^2}, \quad (2)$$

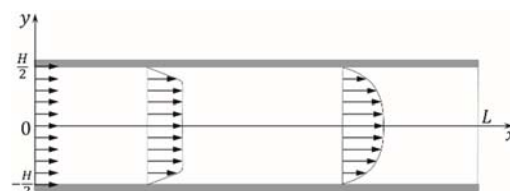


Fig. 1. A steady-state laminar spatially developing channel flow.

where u and v are the velocity components in the x and y directions, ρ is the density and ν is the kinematic viscosity. At a location x , we integrate Eq. (2) in the y direction from $y = -H/2$ to $H/2$, *i.e.* from the bottom wall to the top wall to obtain,

$$\int_{-H/2}^{H/2} \frac{\partial(uu)}{\partial x} dy = -\frac{1}{\rho} \frac{\partial}{\partial x} \int_{-H/2}^{H/2} p dy + \nu \frac{\partial u}{\partial y} \Big|_{y=H/2} - \nu \frac{\partial u}{\partial y} \Big|_{y=-H/2}. \quad (3)$$

During the integration, the second term on the left hand side of Eq. (2) has been eliminated because no-slip condition on the wall. The integral of the second term on the right hand side of Eq. (2) is also eliminated because the mass flow rate through the channel $\dot{m} = \int_{-H/2}^{H/2} \rho u W dy = \rho u_b H W$ is a constant, where u_b is the bulk fluid velocity. We can further simplify Eq. (3) to

$$c_1 u_b^2 = -\frac{H}{\rho} \frac{\partial \bar{p}}{\partial x} + \nu \frac{\partial u}{\partial y} \Big|_{y=H/2} - \nu \frac{\partial u}{\partial y} \Big|_{y=-H/2}, \quad (4)$$

by introducing the following notations,

$$c_1 = \frac{\int_{-H/2}^{H/2} \frac{\partial(uu)}{\partial x} dy}{u_b^2}, \quad (5)$$

$$\bar{p} = \frac{1}{H} \int_{-H/2}^{H/2} p dy. \quad (6)$$

The viscous wall stress terms in Eq. (4).

$$\tau_w = \mu \frac{\partial u}{\partial y} \Big|_{y=\pm H/2}, \text{ can be expressed in terms of}$$

the Reynolds number $Re = u_b H / \nu = \dot{m} / \mu W$ for fully developed laminar channel flows (Pritchard (2011)),

$$C_f = \frac{\tau_w}{\frac{1}{2} \rho u_b^2} = \frac{12}{Re}. \quad (7)$$

Using fully developed condition for the evaluation of the viscous wall stress terms is a significant approximation involved in this analysis. Combining Eqs. (4) and (7), we obtain the following equation,

$$\frac{\partial \bar{p}}{\partial x} = -\frac{c_1}{\rho H^3} \dot{m}^2 - \frac{12\mu}{\rho H^3 W} \dot{m}. \quad (8)$$

The pressure drop after a distance of l in the flow direction is then estimated by integrating Eq. (8) in the flow direction,

$$\Delta \bar{p} = -\frac{\int_0^l c_1 dx}{\rho H^3} \dot{m}^2 - \frac{12\mu l}{H^3} \dot{m}. \quad (9)$$

Eq. (9) can be re-written as,

$$\Delta \bar{p} = a^* \dot{m}^2 + b^* \dot{m}, \quad (10)$$

where

$$a^* = -\frac{\int_0^l c_1 dx}{\rho H^3}, b^* = -\frac{12\mu l}{H^3} \quad (11)$$

Here we use notations a^* and b^* in Eq. (10), which are derived based on the flow equations. The model constants in the empirical model in Eq. (1) are differentiated as a and b . For clarity, we call Eq. (10) as the derived model as opposed to the empirical model referred to in Eq. (1). It is noted that Eqs. (9) and (10) are not exactly valid since several

assumptions are involved in the derivation. We have also forced the convection term to look like the quadratic term in Eq. (10) with the assumption that a^* is not strongly dependent on \dot{m} (to be examined in detail later). Nevertheless, the expressions in Eqs. (9) and (10) are in the same form as the empirical model in Eq. (1). This provides a theoretical support to the empirical model expressed in Eq. (1). The assumptions involved in the derivation of Eq. (9) are summarized as follows: 1) Steady state; 2) Laminar flow; 3) Incompressible flows; 4) Constant transport properties; 5) Friction coefficient C_f in Eq. (7) based on fully developed channel flows.

In the empirical model, the model constants a and b are not dependent on the mass flow rate \dot{m} . From Eq. (11), we can see that b^* is independent of \dot{m} with the above assumptions while a^* is mostly not. It is important to examine the dependence of a^* on \dot{m} because it directly affects the accuracy of the model and this will be conducted in the following discussion. From Eqs. (1), (5) and (10), we can see that the quadratic term in the derived model in Eq. (10) is from the convection term and the linear term is from the viscous term. When the channel flow becomes fully developed, the quadratic term vanishes and the model is exact.

2.2 Remarks on General Internal Flows

For the steady state laminar channel flow in Fig. 1, we are able to perform the integral analysis in Section 2.1 to find the basis of the empirical model in Eq. (1) after introducing a number of assumptions. For variable area channel flows, we can perform a similar analysis to obtain an equation for the pressure drop in the same form as the empirical model in Eq. (1) with some additional assumptions: 1) Flow is primarily in the x direction; 2) The radius of curvature of channel walls is large enough so that $\left| \frac{\partial}{\partial \hat{n}} \right| \approx \left| \frac{\partial}{\partial y} \right|$, where \hat{n} is the normal direction of the wall. Given the empirical nature of the model in Eq. (1), we do not show this analysis. For more general flows (e.g., transient flows, compressible flows, variable transport properties), the analysis in Section 2.1 can be extended as well, but will lead to more complicated model formulations. The empirical model in Eq. (1) captures the leading order effect of flows and if high-order effect is needed, the model naturally becomes more complicated. We are not aware of much interest in more complicated models in real-life engineering applications and hence the focus of this work is on the empirical model with the leading order effect in Eq. (1).

For turbulent flows, a similar analysis can be performed. The major difference is that for turbulent flows, the viscous wall scaling is different from laminar flows and Eq. (7) is not applicable. For turbulent rectangular duct flows, a wall scaling of $C_f \sim Re^{-0.25}$ is proposed in Dean (1978). With this scaling, a model of form $\Delta \bar{p} = a^* \dot{m}^2 + b^* \dot{m}^{1.75}$ can be derived. In general, if we assume a wall scaling of $C_f \sim Re^{-2+\beta}$ with β a constant, we obtain a model in

the form of $\Delta p = a^* \dot{m}^2 + b^* \dot{m}^\beta$ which is a generalized version of the empirical model in Eq. (1). In this work, we only consider the special case $\beta = 1$ due to the empirical nature of the model. It will be shown in the later discussions that the second term $b\dot{m}^\beta$ in the generalized empirical model is negligible in high Re number flows so that the accuracy of the model is not sensitive to the value of β .

After having established the theoretical basis of the empirical model in Eq. (1), in a limited sense, we now assess the model accuracy and uncertainty in the following sections. In the empirical model in Eq. (1), the coefficients a and b are constant, *i.e.*, they are independent of the mass flow rate \dot{m} . From Eq. (11) we can see that the coefficient b^* for the linear term depends on the geometry and transport property and hence is independent of \dot{m} while the coefficient a^* for the quadratic term is dependent on \dot{m} because the normalized convection term cI defined in Eq. (5) is dependent on \dot{m} . Such dependency will be examined in detail in the following Section 3 in the laminar channel flow. The performance of the empirical model will then be examined in Section 4 in several test cases including two laminar channel flows with variable areas, a turbulent channel flow and a complicated flow involving turbulent flow through the underhood of a car.

3. DEPENDENCE OF THE COEFFICIENT a^* ON MASS FLOW RATE

In the empirical model in Eq. (1), both coefficients a and b are assumed to be independent of \dot{m} . As discussed above, in the laminar channel flow, although b^* in the derived model does not depend on \dot{m} , the coefficient a^* does. It is important to understand such dependency to help estimate the accuracy of the empirical model. As can be expected, the coefficient a^* must have a weak dependence on \dot{m} in order for the model to have reasonable accuracy. If this is not the case, *i.e.*, a^* strongly depends on \dot{m} , the accuracy of the empirical model is generally expected to be poor. In this section, we test the dependence of the model coefficient a^* on \dot{m} based on the CFD simulation results of the developing laminar channel flow.

3.1 Simulation of Laminar Channel Flow

The CFD simulations of the 2D laminar channel flow are performed in ANSYS FLUENT 14.5 (Fluent, 2009). The computational domain is chosen to cover the air flow inside the channel as shown in Fig. 1 with the ratio of the length of the channel L to the height of the channel H , $L/H = 200$. A uniform inflow velocity profile is imposed at the inlet of the channel

and a pressure-outlet boundary condition is imposed at the outlet. The no-slip boundary condition is specified at both walls. The Reynolds number, $Re = u_b H / \nu$, varies from 1 to 2000 corresponding to the mass flow rate \dot{m} varying from 0.01 kg/s to 20 kg/s. The pressure-velocity coupling is treated with the SIMPLE algorithm and the spatial discretization for the convection terms is done using a second-order accurate upwind scheme. The convergence criterion is set to be less than 10^{-6} for the residuals. The convergence and accuracy of the laminar channel flow simulations are verified in Fig. 2. In the figure, a case with the highest Re considered above ($Re = 2000$) is tested. Six grids are considered with the number of grid nodes, 4000 (Grid 1), 9000 (Grid 2), 16000 (Grid 3), 25000 (Grid 4), 100000 (Grid 5) and 200000 (Grid 6). The left plot of Fig. 2 shows the profile of the component of velocity parallel to the x direction, u , at the channel exit ($x/H = 200$) with three different grids, Grid 3, Grid 4 and Grid 5.

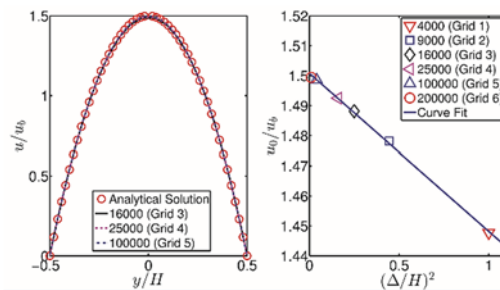


Fig. 2. The velocity profiles u/u_b at the channel exit $x/H = 200$ with different grids (left) and the convergence of the centerline velocity u_0/u_b at the channel exit where Δ is the nominal grid size (right).

The analytical solution of a fully developed channel flow at the same $Re = 2000$ is also shown in the figure as circles. Very close agreement is observed between the simulations and the analytical solution, indicating a fully developed condition at the channel exit. The grid convergence of the centerline velocity u_0 at the channel exit is shown in the right plot of Fig. 2. Second-order grid convergence is evidently observed of the simulation results which is consistent with the second-order accurate schemes used in the simulations. In the following discussions, Grid 4 with 25000 nodes is employed for all the straight laminar channel flow simulations with which less than 1% error is incurred based on the convergence results in Fig. 2. A total number of 500 nodes are used in the stream-wise direction and 50 nodes in the cross-stream direction.

For the analysis of the FLUENT simulation results, we measure the pressure drop $\Delta \bar{p}$ in Eq. (6) over a distance of H around a location x , *i.e.*, measuring the pressure difference $\Delta \bar{p}$ between $x/H \pm 1/2$. The

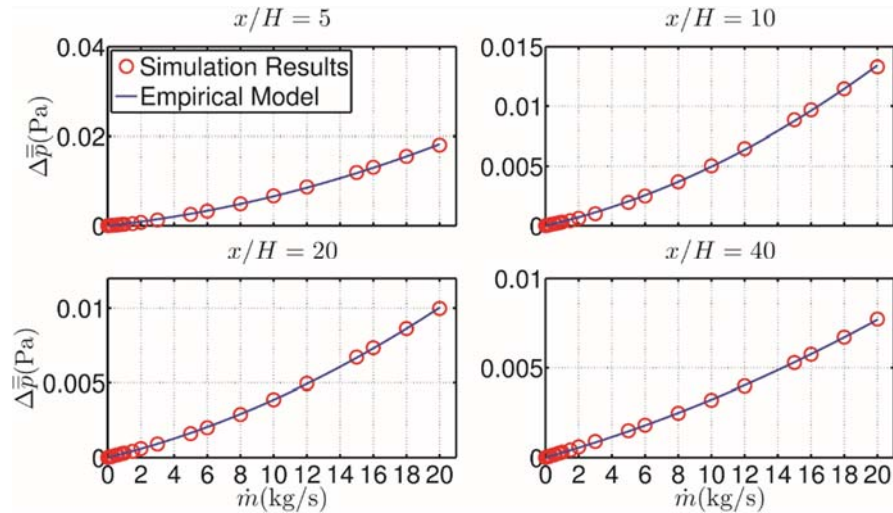


Fig. 3. The pressure drop $\Delta\bar{p}$ between $x/H \pm 1/2$ at the different stream-wise locations, $x/H = 5, 10, 20$ and 40 , in the laminar channel flow.

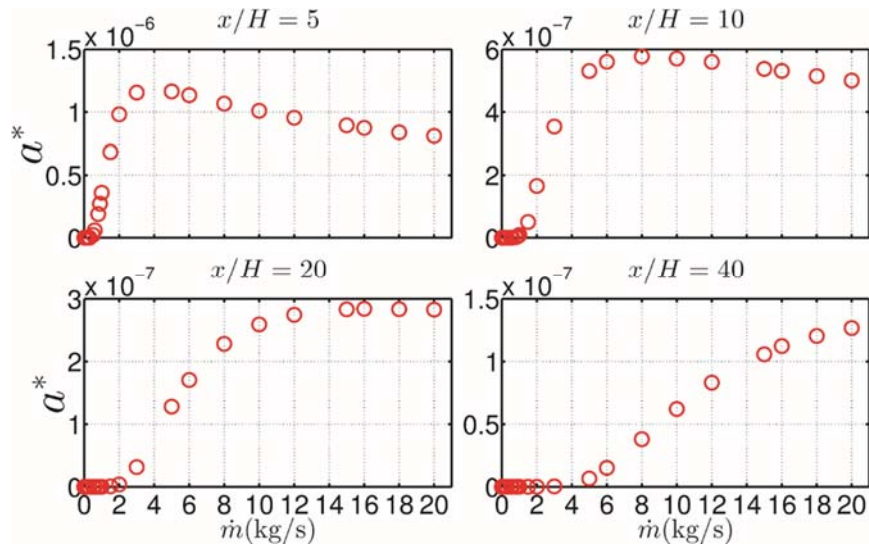


Fig. 4. The coefficient a^* defined in Eq. (11) at the different stream-wise locations, $x/H = 5, 10, 20$ and 40 , in the laminar channel flow, computed from the FLUENT simulation results.

simulated results for $\Delta\bar{p}$ against \dot{m} at the different stream-wise locations, $x/H = 5, 10, 20$ and 40 are shown as circles in Fig. 3. The simulation results are fit to the empirical model in Eq. (1) which is represented by solid line in Fig. 3. From the figure, we can see that the model fit is in excellent agreement with the simulation results with a maximum relative difference of 1%. Here the relative difference is defined as, $(\Delta p - \Delta\bar{p})/\max(\Delta\bar{p})$, where Δp is the empirical model result based on Eq. (1), $\Delta\bar{p}$ is the FLUENT simulation result and $\max(\Delta\bar{p})$ is the maximum value of the pressure drop from the simulations in the entire range of massflow rates that are computed. The relative difference between the CFD results and the empirical model indicates a good accuracy of the empirical model for the laminar channel flow. This seems to

suggest that the coefficient a^* in Eq. (11) in the laminar channel flow does not have a strong dependency on \dot{m} as having been assumed in the empirical model. We evaluate this independency using the simulation results for the laminar channel flow in the following Section 3.2.

3.2 Dependence of a^* on \dot{m}

The dependence of the coefficient a^* in Eq. (11) on \dot{m} is examined in Fig. 4 where the values of a^* computed from the simulation results are plotted against \dot{m} . When \dot{m} is relatively small, the flow may reach fully developed, e.g., for $\dot{m} < 2$ kg/s at $x/H = 20$. As a result, $a^* = 0$ in Eq. (10) because of the fully developed condition. When \dot{m} increases, the flow moves from fully developed to developing stage at a specified location and the value of a^* increases, e.g., when $\dot{m} > 3$ kg/s at $x/H = 20$ in Fig.

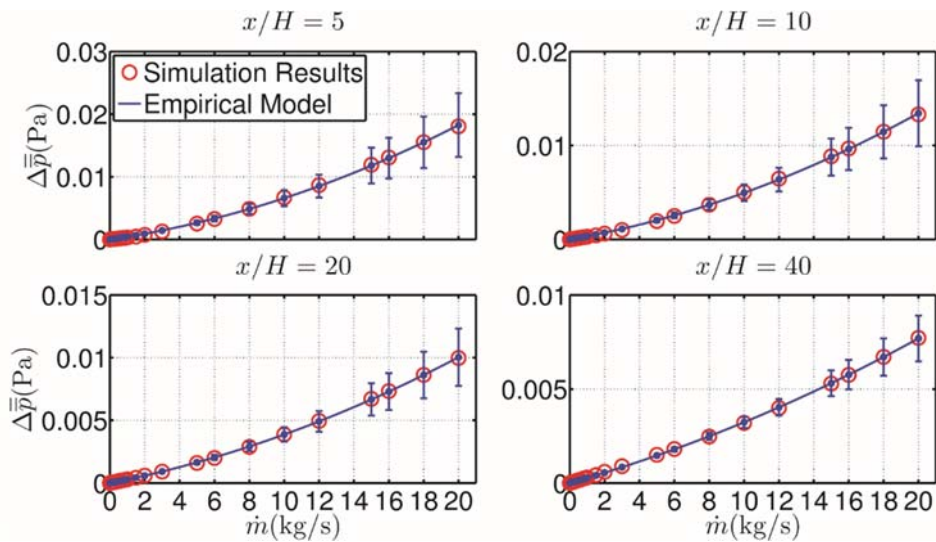


Fig. 5. The sensitivity of the empirical model to the perturbation $\varepsilon = 0.5$ of the model coefficient a in Eq. (1) at the different stream-wise locations, $x/H = 5, 10, 20$ and 40 , in the laminar channel flow.

4. When \dot{m} is large enough, further increasing \dot{m} can cause some slight decrease of a^* , e.g., when $\dot{m} > 8$ kg/s at $x/H = 10$ in Fig. 4. The results in Fig. 4 show a strong dependence of a^* on \dot{m} , which contradicts our speculation discussed in Section 3.1. Despite the fact that a^* has a strong dependence on \dot{m} as shown in Fig. 4, the empirical model performs excellently well as shown in Fig. 3. This creates a puzzle about the model accuracy and the unexpected dependence of a^* on \dot{m} . To gain deep insights into the puzzling results in the laminar channel flow, we perform a sensitivity analysis of the empirical model and examine the characteristics of the flows under different mass flow rate \dot{m} in the following Section 3.3.

3.3 Sensitivity Analysis and Characterization of Flows

The sensitivity of the model is examined by perturbing the coefficient a in Eq. (1) by a factor of $1 \pm \varepsilon$, where ε is the sensitivity input. The effect of the perturbation on the model accuracy is then analyzed. The sensitivity results based on the FLUENT simulation results for the channel flow are shown in Fig. 5 where the simulation results are shown as circles and the empirical model results are shown as solid lines with error bars. The sensitivity input is $\varepsilon = 0.5$ and the error bars in Fig. 5 show the absolute deviation $[\Delta\bar{p} - \sigma^-, \Delta\bar{p} + \sigma^+]$ of the empirical model given the sensitivity input, where σ^- and σ^+ show the deviation. The results in the figure show that the error bar size at the relatively low mass flow rate is small while it becomes larger at the relatively large mass flow rate. The results suggest a monotonic increase of the sensitivity of the empirical model to the model coefficient a when the mass flow rate \dot{m} is increased. This monotonic increase of the sensitivity is confirmed in Fig. 6 where the error bar size $\sigma = \sigma^- + \sigma^+$ against \dot{m} is shown for three different sensitivity inputs $\varepsilon = 0.5$,

1.0, and 2.0. This sensitivity behavior needs more exploration which is delayed till Section 3.4. At this point, given the sensitivity results in Figs. 5 and 6, we can readily explain the puzzle we observed in Section 3.2. In the region where the coefficient a^* varies significantly at low mass flow rate as shown in Fig. 4, it turns out that the model is quite insensitive to the variation of a . In this case, even though the model coefficient a^* is not constant as can be seen in Fig. 4, the accuracy of the empirical model is not significantly compromised because of the lesser sensitivity of the model to the perturbation of a at the relatively low mass flow rates. In the region where the coefficient a^* varies only slightly, corresponding to the relatively large mass flow rates, the empirical model's accuracy is expected to be good because of the approximate constant value of the model coefficient a^* in this region. This observation clearly solves the puzzle we encountered in Section 3.2 as to why the empirical model performs so well even though the model coefficient a^* is found to vary significantly. This finding provides a better understanding of the empirical model. From the sensitivity analysis we also observed two distinct regions in which the empirical model behaves differently. The two distinct regions, a convection dominated region and a diffusion dominated region are explored in the following Section 3.4.

3.4 Convection Dominated and Diffusion Dominated Flows

To understand the two distinct regions of the model's behavior discussed in Section 3.3 and the reason for having them, we examine the model further in Fig. 7. In the figure, the two individual terms of the empirical model are plotted separately along with the model fit itself. From the figure, we can see that the relative magnitudes are quite different for different values of \dot{m} . When \dot{m} is relatively small, e.g., $\dot{m} < 10$ kg/s at $x/H = 5$ in Fig. 7, the square term $a\dot{m}^2$ is much smaller than the

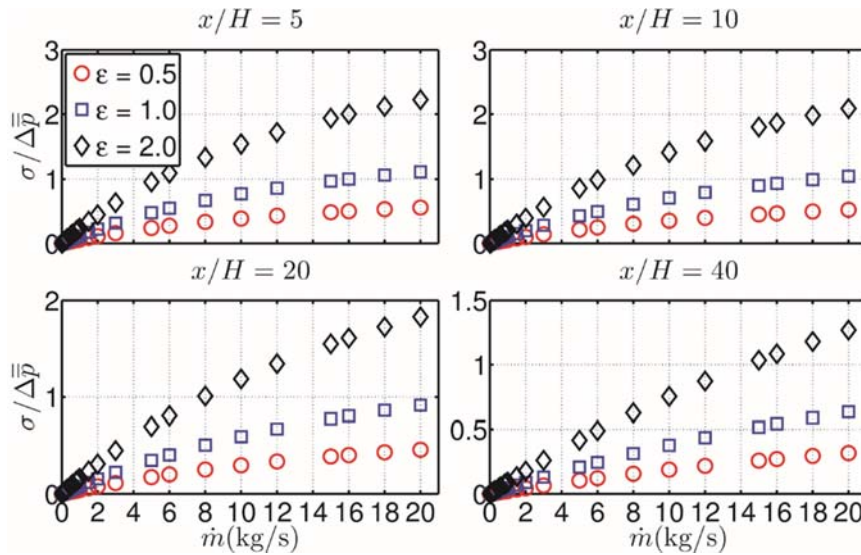


Fig. 6. The model sensitivity σ against the mass flow rate \dot{m} for the different sensitivity input $\varepsilon = 0.5$ (circles), 1.0 (squares), 2.0 (diamonds), at the different stream-wise locations, $x/H = 5, 10, 20$ and 40, in the laminar channel flow.

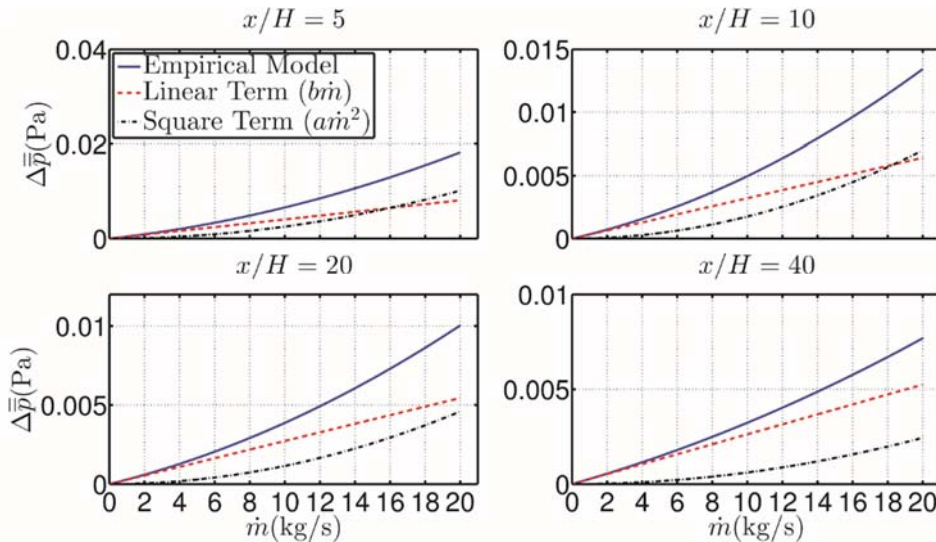


Fig. 7. The variation of the square term $a \dot{m}^2$ and linear term $b \dot{m}$ against the mass flow rate \dot{m} at the different stream-wise locations, $x/H=5, 10, 20$ and 40, in the laminar channel flow.

linear term $b \dot{m}$, while when \dot{m} is relatively large, e.g., $\dot{m} > 20$ kg/s at $x/H = 5$ in Fig. 7, the square term is much larger than the linear term. This creates two distinct regions of the model's behavior as discussed in Section 3.3. In one region where \dot{m} is relatively small, the linear term dominates and the model performs quite well even if in this region the quadratic term coefficient a^* varies significantly as shown in Fig. 4. In the other region where \dot{m} is relatively large, the quadratic term dominates and the model also performs quite well because in this region the quadratic term coefficient is approximately constant (or at least varies only slightly) as shown in Fig. 4. Since the quadratic term comes from the convection term and the linear term comes from the diffusion term as discussed in Section 2.1, we

characterize the two distinct regions as a diffusion-dominated flow region and a convection-dominated flow region. The two characteristic flow regions are illustrated in Fig. 8.

In summary, in Section 3, we examined the dependence of the coefficient a^* on the mass flow rate. This coefficient is related to the coefficient a in the empirical model in Eq. (1). It is found that in the simple channel flow, the empirical model performs excellently well while a^* is strongly sensitive to the mass flow rate. This creates a puzzle since a constant model coefficient a is used when examining the model. The puzzle is successfully solved by performing a sensitivity analysis of the empirical model to the coefficient a . The analysis reveals that there are two distinct regions where the model behaves completely different. Although the

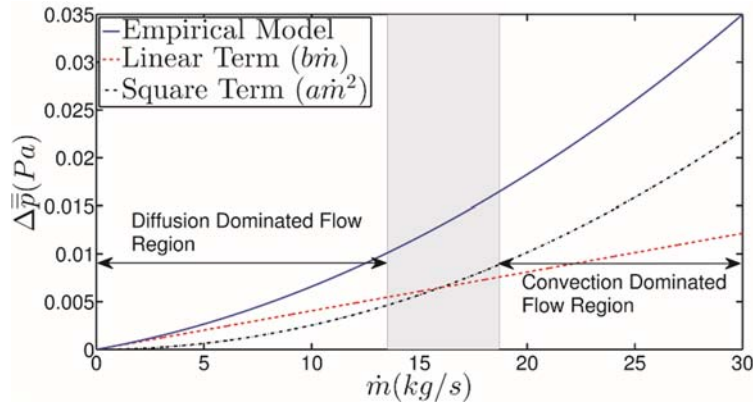


Fig. 8. The diffusion dominated flow region and the convection dominated flow region. The model fit results are taken at $x/H=5$ in the laminar channel flow.

model shows consistent performance over a wide range of mass flow rates, the reason for getting such a good performance is actually different for different mass flow rates due to the existence of the two distinct regions of the model. This provides a thorough understanding of this empirical model that is in simple form yet not simple for a complete understanding.

It is noted that the above discussion is limited to a simple channel flow. In more complicated flows, the analysis is more involved and the model is probably not as accurate as in the channel flow. Nevertheless, the analysis is very useful for providing a theoretical basis to the model and for providing a complete understanding of the model. In the following Section 4, we provide a quick examination of the performance of the empirical model in several more complicated internal flows with the aim to provide a brief assessment of the general applicability of the model to a wider range of flows. In the examination, we use CFD simulation results to fit the empirical model for the assessment.

4. APPLICATION OF MODEL TO SAMPLE INTERNAL FLOWS

Four more internal flows are considered in this section to demonstrate the applicability of the empirical model in Eq. (1): a laminar flow inside a converging channel, a laminar flow inside a curved channel, a turbulent channel flow and a complicated turbulent flow through the hood of a car.

4.1 Laminar Flow inside a Converging Channel

A converging channel is considered which represents a more challenging case than the straight channel since the flow can never reach fully developed state. The converging channel considered in this work is shown in Fig. 9. The length of the channel is L and the height of the channel is $H(x)$ at a stream-wise location x . The channel geometry is defined as $H(0)/H(L) = 2.5$ and $L/H(L) = 5$. The angle of inclination of the wall with the horizontal is $\theta = 8.53^\circ$. The average channel height is $H_m = (H(0)+H(L))/2$

and $L/H_m = 2.857$. Unit width is considered in the span-wise direction, $W = 1\text{m}$. The working fluid is air at room temperature. The computational domain covers the fluid flow region inside the channel. The grid generated in ICEM CFD (ICEM-CFD (2009)) has a total number of 20000 nodes with 200 nodes in the y direction and 100 nodes in the x direction. A uniform velocity boundary condition, u_{in} , is defined at the inlet of the channel and a pressure-outlet boundary condition is defined at the outlet of the channel. No-slip boundary condition is specified at both walls. The Reynolds number, $Re = u_{in}H_m/\nu$, varies from 1.75 to 14 corresponding to the mass flow rate \dot{m} from 2.5 kg/s to 20 kg/s. The solution algorithm and the convergence criterion are the same as in the straight channel case in Section 3.1. To examine the accuracy of the empirical model for the converging laminar channel flow, we define $\Delta\bar{p}$ to be the pressure drop between $x/H_m \pm 0.15$, where H_m is the average height.

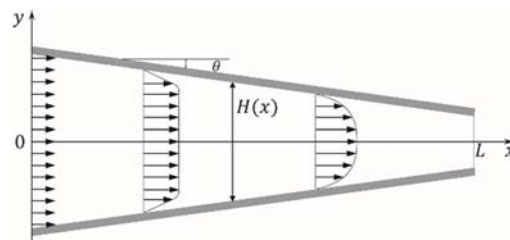


Fig. 9. A steady-state laminar spatially developing flow through a converging channel.

The computed values of $\Delta\bar{p}$ in the converging laminar channel flow are shown as open circles in Fig. 10 at the four different locations in the stream-wise direction, $x/H_m = 1, 1.5, 2$ and 2.5 . The simulation results are then fit into the empirical model in Eq. (1) which is shown as the solid lines in the figure along with the error bars that correspond the sensitivity input $\epsilon = 0.5$. From the figure we can see that the model performs exceptionally well for the flow conditions that are considered. The results from the converging laminar channel flow are

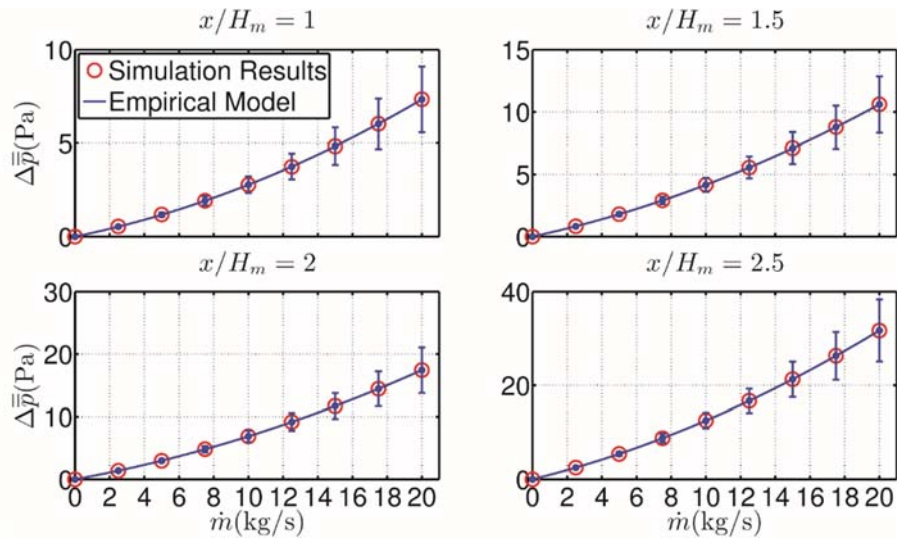


Fig. 10. The pressure drop $\Delta \bar{p}$ between $x/H_m \pm 0.15$ at the different stream-wise locations, $x/H_m = 1, 1.5, 2$ and 2.5 , for the laminar converging channel flow along with the error bars for $\varepsilon = 0.5$.

qualitatively similar to those from the straight channel in Fig. 3. Specifically, the results are insensitive to the model constant a for the small mass flow rates and the sensitivity grows when the mass flow rate is increased. The excellent performance of the empirical model can be explained by the same reasons explored in the straight channel in Section 3.

4.2 Laminar Flow inside a Curved Channel

A laminar flow with more complicated geometry is further considered as shown in Fig. 11. The profile of the wall is specified according to,

$$H(x) = \pm \frac{H_{in}}{2} \left[1 + d_1 \times \sin\left(d_2 \frac{x}{H_{in}} 2\pi\right) \right], \quad (12)$$

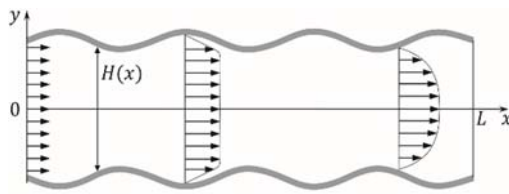


Fig. 11. A steady-state laminar spatially developing flow through a curved channel.

where H_{in} is the height of the channel at the inlet and d_1 and d_2 are constants. For this study, the values are specified to be $d_1 = 0.2$, $d_2 = 0.6$ and $H_{in} = 4\text{m}$. The average height of the channel given by $H_m = 1/L \int_0^L H(x) dx$ is also 4m. The L/H_m ratio for the channel is 8.6375. The computational grid for this flow in FLUENT has 99301 cells. With the Reynolds number defined as $Re = u_{in} H_m / \nu$, the Reynolds number varies from 2 to 20 corresponding to the mass flow rate \dot{m} from 2 kg/s to 20 kg/s.

Similar to the converging channel in Section 4.1, we measure the pressure difference $\Delta \bar{p}$ across the two streamwise locations $x/H_m \pm 0.15$, at four different axial locations $x/H_m = 3.5, 4, 4.3$ and 4.7 . These locations are selected to capture the different features of the periodic channel. The simulation results along with the model fit for the curved channel are shown in Fig. 12. From the figure, again we observe excellent performance of the empirical model despite its simplicity. It is suggested that the empirical model examined in this work can probably be used in many laminar internal flows with good accuracy. In the following section, we examine two turbulent cases to further demonstrate the performance of the simple empirical model.

4.3 Turbulent Channel Flow

A turbulent straight channel flow is considered. The channel has the same geometry as the laminar one as shown in Fig. 1, with $L/H = 200$. The Reynolds number, $Re = u_{in} H / \nu$ varies from 7000 to 200000 corresponding to the mass flow rate \dot{m} from 0.7 kg/s to 20 kg/s. The grid generated for the FLUENT simulation has 39601 cells. Turbulence is modeled using the Reynolds Stress Transport model (RST) with the standard wall function model in FLUENT (Fluent (2009)). The turbulence intensity at the in-let and outlet is set to 5% and the turbulent length scale to H .

We validate the CFD simulations by using Direct Numerical Simulation (DNS) results for a fully developed turbulent channel flow with $Re_\tau = 590$ (Moser *et al.* (1999)). The length of channel in the current simulations is sufficiently long to reach the fully developed state at the exit $x/H = 200$. For $Re = 21500$, the Reynolds number $Re_\tau = u_\tau(H/2)/\nu = 592.5$ based on the friction velocity u_τ (Pope (2001)) and channel half-width is close to

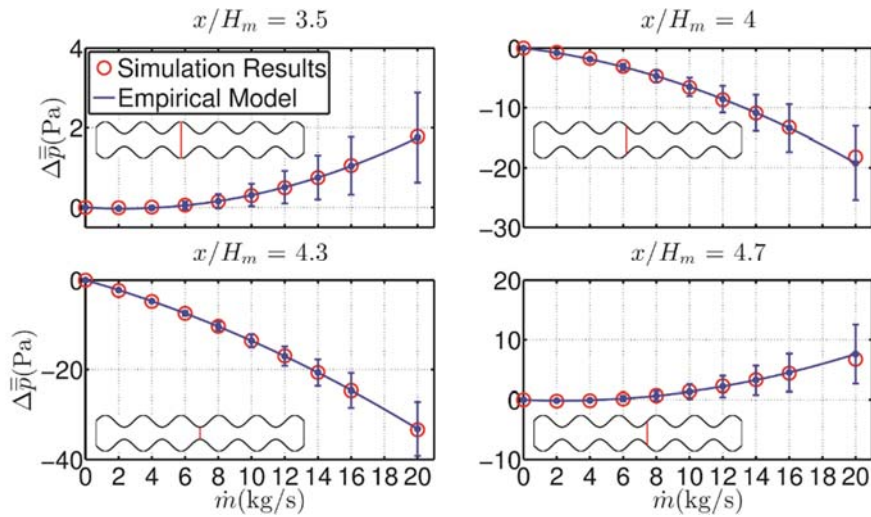


Fig. 12. The pressure drop $\Delta \bar{p}$ between $x/H_m \pm 0.15$ at the different stream-wise locations, $x/H_m = 3.5, 4, 4.3$ and 4.7 , for the laminar curved channel flow along with the error bars for $\varepsilon = 0.5$.

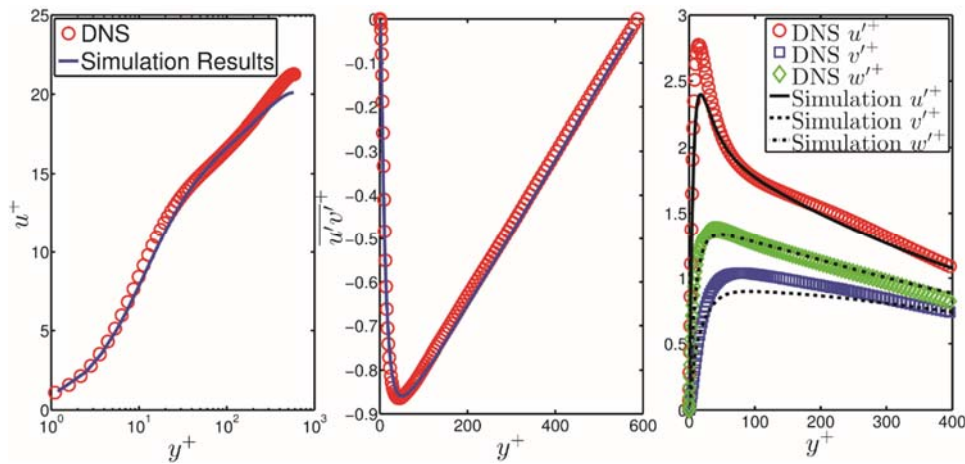


Fig. 13. The mean velocity u^+ in terms of wall units for fully developed turbulent channel flow (left).

The Reynolds stress component $\overline{u'v'^+}$ velocity in terms of wall units for fully developed turbulent channel flow (center). The components of root mean square velocity u'^+, v'^+ and w'^+ in terms of wall units for fully developed turbulent channel flow (right).

the DNS Re_τ . The leftmost plot in Fig. 13 compares the profile of the predicted mean velocity u^+ in the wall units with the DNS results. It can be observed that the predicted mean velocity profile is in good agreement with the DNS results, including the near wall region. The center and the rightmost plots in

Fig. 13 compare the Reynolds shear stress $\overline{u'v'^+}$ and the root mean square (RMS) velocity profiles u'^+, v'^+, w'^+ respectively. The simulated shear stress and RMS velocities match the DNS results well with the maximum relative error of 14%. The good agreement with the DNS data evidently validates the current FLUENT simulations. The same level of accuracy is expected for other Re that is considered, and this accuracy is adequate for the purpose of this study.

The mean pressure drop $\Delta \bar{p}$ is measured over a

distance of H at $x/H \pm 1/2$. The simulated values of $\Delta \bar{p}$ from the FLUENT simulations are plotted against \dot{m} as circles at the different stream-wise locations, $x/H = 5, 10, 20$ and 40 in Fig. 14. The performance of the empirical model in the turbulent channel flow is similar to the laminar flows above. The maximum relative error of the empirical model defined in Section 3.1 is estimated to be about 3% in the turbulent channel flow in Fig. 14 which demonstrates the applicability of the empirical model to turbulent flows.

4.4 Turbulent Flow through Underhood of Car

Lastly, we examine the application of the empirical model in Eq. (1) in a practical application with a very complicated geometry, the flow through the underhood of a car (Pant *et al.* (2013), Pant (2014)),

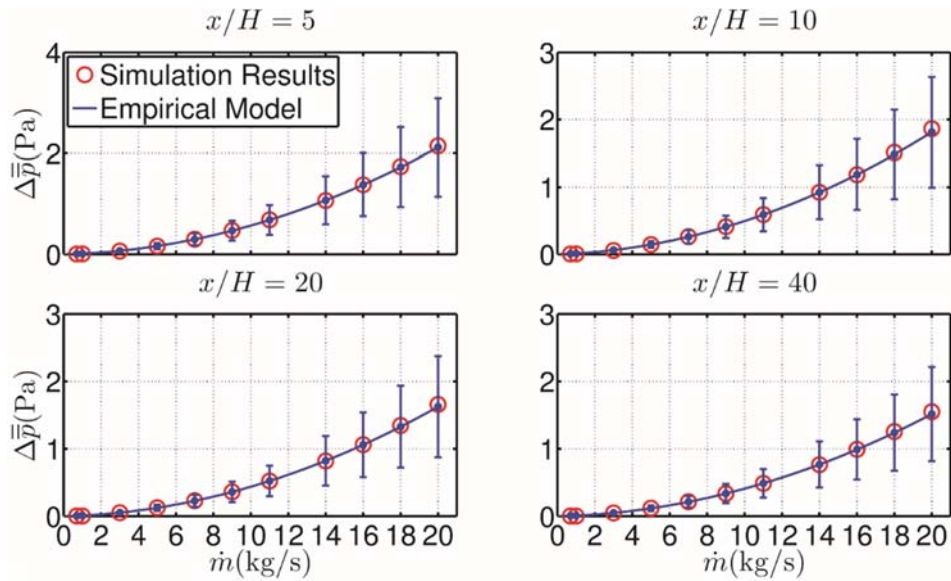


Fig. 14. The mean pressure drop $\Delta \bar{p}$ between $x/H_m \pm 1/2$ at the different stream-wise locations, $x/H = 5, 10, 20$ and 40 , for the turbulent straight channel flow along with the error bars for $\varepsilon = 0.5$.

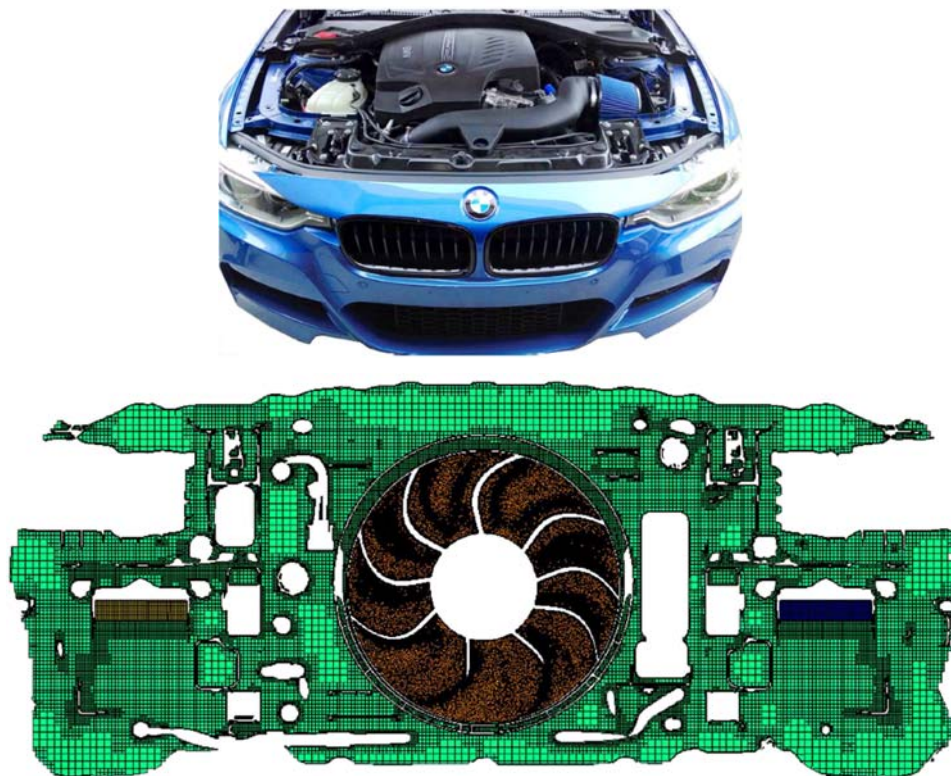


Fig. 15. Underhood architecture of car model A (top). Section of the 3D volume mesh passing through the suction fan (bottom). The normal of the section plane points in the direction of the motion of the car.

with the goal to further demonstrate the applicability of the model to flows that are more complicated than those examined in Sections 4.1 - 4.3. Two geometrically very different car models, BMW F30 sedan (model A) and Mini Cooper R56 hatchback (model B) with widely different underhood architecture are considered to examine the performance of the model. The underhood of a car primarily consists of the engine compartment, the

cooling module and the air intake grill as can be seen in the top image in Fig. 15. The engine compartment houses the engine block and the gearbox. The cooling module consists of a set of heat exchangers and a suction fan. The air intake grill is used for directing air into the underhood and some auxiliary components of the engine. Underhood thermo-flow analysis is needed for designing an efficient engine cooling system for

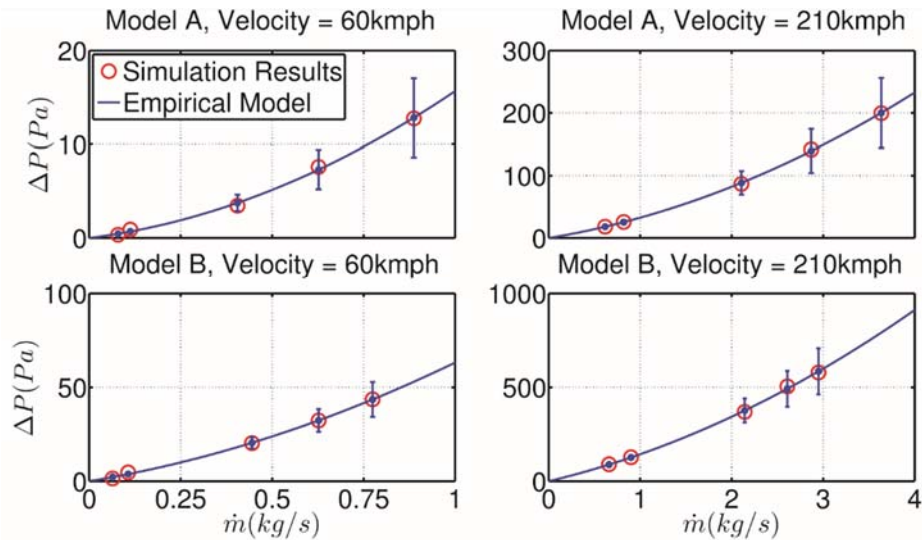


Fig. 16. The mean pressure drop across the underhood of two different car models A and B at the speed of 60kmph and 210kmph along with the error bars for $\epsilon = 0.5$.

maximizing its performance in variable conditions. For the analysis of the underhood flow, the empirical model in Eq. (1) is used to establish the relation between the pressure drop across the inlet and outlet of the underhood and the mass flow rate of the air flowing through it. Due to the complexity of the structure of the underhood, the flow can hardly be described as a channel flow. Nevertheless, it is important to have a quantitative examination of the accuracy of the empirical model in this complicated flow.

The CFD simulations of the underhood flow were performed using the commercial CFD tool, STAR-CCM (STAR-CCM (2011)) at BMW AG, Munich and the simulation data are used here for our analysis. In the CFD simulation, a detailed geometric model of the car is placed inside a rectangular box to simulate the effect of a wind tunnel. The total number of cells is about 50 million with the majority of the cells concentrated in the underhood region. The bottom plot in Fig. 15 shows a section of the volume mesh passing through the suction fan in the cooling module. The normal of the section plane points in the direction of motion of the vehicle. About 50% of the total cells are in the underhood flow region. The total computational cost for one simulation is around 12 hours on 96 processor cores (1152 cpu-hours in total per simulation). The turbulence is modeled using the $k - \epsilon$ model and the standard wall function is used. A range of mass flow rate from 0 to 4 kg/s is considered. A uniform velocity inlet boundary condition is specified and a 10% turbulence intensity is specified with the ratio of the turbulent to the molecular viscosity set to 10 at the inflow. A pressure outlet boundary condition is specified. The RANS simulations have known to show good agreement with the experimental results with regards to massflow through the underhood (Pant *et al.* (2013), Pant (2014)).

In order to calculate the pressure drop ΔP , two sections are defined at the inlet and outlet of the underhood. ΔP is the difference between the area

averaged pressure over these two surfaces. The variation of the simulated values of ΔP with \dot{m} for two widely different car models, A and B is shown in Fig. 16. Two different vehicle speeds, 60 and 210 kilometers per hour (kmph) are considered. From the figure, we can see that the empirical model provides a good fit to the simulation data despite the simplicity of the model. This clearly demonstrates the performance and applicability of the empirical model to complicated flows such as the flow through the underhood. When compared to the other flows discussed in Sections 3 and 4, the empirical model in Fig. 16 also shows similar sensitivity to the sensitivity input $\epsilon = 0.5$.

To summarize, we examined the accuracy and sensitivity of the empirical model in Eq. (1) in four different flows in this section, a laminar flow in a converging channel in Section 4.1, a laminar flow in a curved channel in Section 4.2, a turbulent flow in straight channel in Section 4.3 and a complicated turbulent flow through a car hood. The results strongly support the wide applicability of the empirical model despite the simplicity of the model.

5. CONCLUSION

In this work, a theoretical analysis is conducted of a simple empirical model that relates the pressure drop and the mass flow rate in internal flows in order to provide a theoretical basis for the model. An integral analysis based on the Navier-Stokes equation in laminar developing channel flows yields a model that matches the empirical model well. The model's accuracy is speculated to be largely determined by the dependence of a model coefficient a^* on the mass flow rate. A weak dependence of a^* on the mass flow rate is required in order to yield good accuracy of the empirical model. In the laminar developing channel flow, the model is found to be highly accurate. However, the model coefficient a^* is also found to vary significantly with the mass flow rate which creates a big puzzle in the understanding of the

simple model. Sensitivity analysis of the model is then performed to understand the puzzling results. The results of the sensitivity analysis of the model and the characterization of the flows into diffusion dominated and convection dominated flow regime eventually help us to resolve the puzzle completely. The empirical model is then applied to several more complicated internal flows to demonstrate the applicability of the empirical model. The established theoretical basis for the empirical model and its thorough understanding gained from this work can be expected to be useful in engineering applications involving internal flows.

ACKNOWLEDGMENTS

We are grateful to Dr. Bernhard Zuck, Dr. Marco Schwarze and Mr. Danilo Bruno at BMW AG, Munich for providing us the simulation data for the underhood cooling analysis.

REFERENCES

- Ahmed, N. and D. K. Sunada (1969). Nonlinear flow in porous media. *Journal of the Hydraulics Division Proceedings of the American Society of Civil Engineers* 95, 1847–1857.
- ANSYS, ICEM. (2011). *CFD User Guide*. ANSYS Inc.
- Awbi, H. B. (2008). *Ventilation systems: Design and Performance*. Psychology Press.
- Baker, O. *et al.* (1953). Design of pipelines for the simultaneous flow of oil and gas. In *Fall Meeting of the Petroleum Branch of AIME*. Society of Petroleum Engineers.
- Dean, R. (1978). Reynolds number dependence of skin friction and other bulk flow variables in two-dimensional rectangular duct flow. *Journal of Fluids Engineering* 100(2), 215–223.
- Dukler, A., M. Wicks and R. Cleveland (1964). Frictional pressure drop in two-phase flow: A comparison of existing correlations for pressure loss and holdup. *AIChE Journal* 10(1), 38–43.
- Fluent, ANSYS. (2009). *12.0 Theory Guide*. Ansys Inc, 5(5).
- Ghosh, S., T. Mandal, G. Das and P. Das (2009). Review of oil water core annular flow. *Renewable and Sustainable Energy Reviews* 13(8), 1957–1965.
- Hensen, J. L. and R. Lamberts (2012). *Building performance simulation for design and operation*, pp. 338. Routledge.
- Herwig, H. and B. Schmandt (2013). Drag with external and pressure drop with internal flows: a new and unifying look at losses in the flow field based on the second law of thermodynamics. *Fluid Dynamics Research* 45(5), 055507.
- Junqi, D., C. Jiangping, C. Zhijiu, Z. Yimin and Z. Wenfeng (2007). Heat transfer and pressure drop correlations for the wavy fin and flat tube heat exchangers. *Applied Thermal Engineering* 27(11), 2066–2073.
- Kim, Y., V. Payne, J. Choi and P. Domanski (2005). Mass flow rate of R-410A through short tubes working near the critical point. *International Journal of Refrigeration* 28(4), 547–553.
- Lage, J. L., P. S. Krueger and A. Narasimhan (2005). Protocol for measuring permeability and form coefficient of porous media. *Physics of Fluids* 17(8), 8101.
- Liao, Y., X. Li, W. Zhong and G. Tao (2016). Study of pressure drop-flow rate and flow resistance characteristics of heated porous materials under local thermal non-equilibrium conditions. *International Journal of Heat and Mass Transfer* 102, 528–543.
- Manglik, R. M. and A. E. Bergles (1995). Heat transfer and pressure drop correlations for the rectangular offset strip fin compact heat exchanger. *Experimental Thermal and Fluid Science* 10(2), 171–180.
- Martin, K., R. Reiberer and J. Hager (2006). Modeling of short tube orifices for CO₂. In *International Refrigeration and Air Conditioning Conference at Purdue*.
- Moser, R. D., J. Kim and N. N. Mansour (1999). Direct numerical simulation of turbulent channel flow up to Re = 590. *Physics of Fluids* 11(4), 943–945.
- Muley, A. and R. Manglik (1999). Experimental study of turbulent flow heat transfer and pressure drop in a plate heat exchanger with chevron plates. *Journal of Heat Transfer* 121(1), 110–117.
- Oliveira, J. L. G., J. C. Passos, R. Verschaeren and C. Geld (2009). Mass flow rate measurements in gas-liquid flows by means of a venturi or orifice plate coupled to a void fraction sensor. *Experimental Thermal and Fluid Science* 33(2), 253–260.
- Ouyang, L. and K. Aziz (1996). Steady-state gas flow in pipes. *Journal of Petroleum Science and Engineering* 14(3), 137–158.
- Pant, T. (2014). Study of a generalized empirical model for predicting pressure drop for internal flows. Master's thesis, School of Mechanical Engineering, Purdue University.
- Pant, T., D. Bruno, M. Schwarze and B. Zuck (2013). Development of a one-dimensional air flow path model for flow through the underhood of a car. Technical report, BMW AG, Munich, Germany.
- Payne, V. and D. L. O'Neal (2004). A mass flow rate correlation for refrigerants and refrigerant mixtures flowing through short tubes. *HVAC&R Research* 10(1), 73–87.
- Pope, S. B. (2001). *Turbulent flows*, Chapter 7, pp. 267–269. IOP Publishing.

- Pritchard, P. (2011). Fox and McDonald's Introduction to Fluid Mechanics, Chapter 8, 335–359. Wiley.
- Rodriguez, O. and R. Oliemans (2006). Experimental study on oil–water flow in horizontal and slightly inclined pipes. *International Journal of Multiphase Flow* 32(3), 323–343.
- Shodiya, S., A. Aahar, N. Henry and A. Darus (2012). New empirical correlations for sizing adiabatic capillary tubes in refrigeration systems. In *The 4th International Meeting of Advances in Thermofluids (IMAT 2011)*, Volume 1440, 341–355. AIP Publishing.
- STAR-CCM. (2009). User Guide. Version 4.04. 011.
- Straughan, B. (2010). Structure of the dependence of darcy and forchheimer coefficients on porosity. *International Journal of Engineering Science* 48(11), 1610–1621.
- Wang, C., W. Fu and C. Chang (1997). Heat transfer and friction characteristics of typical wavy fin-and-tube heat exchangers. *Experimental Thermal and Fluid Science* 14(2), 174–186.
- Ward, J. (1964). Turbulent flow in porous media. *Journal of the Hydraulics Division* 90(5), 1–12.
- White, F. M. (2008). Fluid mechanics, Chapter 4, 229–249. McGraw-Hill, New York, NY, USA.